Inorganic Chemistry
Article
pubs.acs.org/IC

Effect of Calcination Conditions on Porous Reduced Titanium Oxides and Oxynitrides via a Preceramic Polymer Route

George Hasegawa,*,[†] Tatsuya Sato,[‡] Kazuyoshi Kanamori,[‡] Cheng-Jun Sun,[§] Yang Ren,[§] Yoji Kobayashi,[†] Hiroshi Kageyama,[†,¶] Takeshi Abe,[†] and Kazuki Nakanishi[‡]

[†]Department of Energy & Hydrocarbon Chemistry, Graduate School of Engineering, Kyoto University, Katsura, Nishikyo-ku, Kyoto 615-8510, Japan

[‡]Department of Chemistry, Graduate School of Science, Kyoto University, Kitashirakawa, Sakyo-ku, Kyoto 606-8502, Japan

[§]X-ray Science Division, Advanced Photon Source (APS), Argonne National Laboratory, Argonne, Illinois 60439, United States

[¶]CREST, Japan Science and Technology Agency, Kawaguchi, Saitama 332-0012, Japan

S Supporting Information

ABSTRACT: A preceramic polymer route from Ti-based inorganic−organic hybrid networks provides electroconductive N-doped reduced titanium oxides (Ti_nO_{2n-1}) and titanium oxynitrides (TiO_xN_y) with a monolithic shape as well as well-defined porous structures. This methodology demonstrates an advantageously lower temperature of the crystal phase transition compared to the reduction of TiO_2 by carbon or hydrogen. In this study, the effect of calcination conditions on various features of the products has been explored by adopting three different atmospheric conditions and varying the calcination temperature. The detailed crystallographic and elemental analyses disclose the distinguished difference in the phase transition behavior with respect to the calcination atmosphere. The correlation between the crystallization and nitridation behaviors, porous properties, and electric conductivities in the final products is discussed.

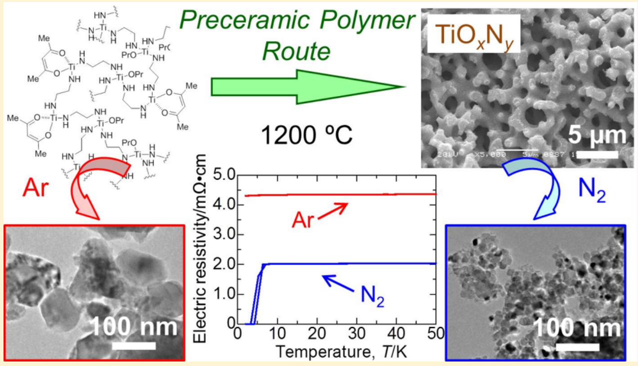

1. INTRODUCTION

In the modern era of interest in electrochemical devices for power and energy storage, electrically conductive materials draw increasing attention in both scientific and industrial fields. Among them, reduced (or substoichiometric) titanium oxides and nitrides have been widely recognized as one of the promising electrode materials in terms of feasibility because these materials are sufficiently abundant, relatively inexpensive, nontoxic, and highly durable.[1−7] The reduction of TiO_2 provides a series of Ti_nO_{2n-1} phases[8−11] involving the Magnéli phases ($n = 4$−10),[12,13] while simultaneous nitridation in the presence of a nitrogen source, such as N_2 and NH_3 involved as the atmosphere, gives rise to cubic-phase titanium oxynitrides (TiO_xN_y)[14] and nitride (TiN).[5,7] The diverse Ti-based materials show various unique characteristics depending on the crystal phase,[15−20] which highlights the importance of controlling the crystal phase. To date, many studies on Ti-based materials in the past have disclosed that the atmospheric conditions during reduction have a significant influence on the phase transition tendency of reduced titanium oxides and oxynitrides.[8,21,22] For instance, the reduction of TiO_2 by Ti metal under vacuum or H_2 yields different polymorphs of Ti_3O_5.[8] The presence of N_2 in the carbothermal reduction of TiO_2 not only leads to nitridation but also gives different crystal transition behavior of reduced titanium oxides.[21,22]

Meanwhile, from the application aspect, it is indispensable not only to control the crystal phase but also to manage the architectural design, such as the morphology and pore property,[23] in order to enhance the effective surface area. Only a few reports, however, demonstrate the design of the nanostructure associated with controlling the crystal phase.[6,7,11,24] Recently, we have developed a new strategy to obtain reduced titanium oxides and oxynitrides with controlled macroporous structure by combining the "preceramic polymer route" and the "phase separation method".[25] The preceramic polymer route is a representative method to manufacture reduced ceramics via carbothermal reduction at high temperature, employing inorganic−organic hybrid compounds (denoted as preceramic polymers, such as polyorganosiloxanes) as the precursor.[26,27] In our method, a well-defined macroporous structure is tailored in the titanium ethylenediamine based preceramic polymers by a sol−gel reaction accompanied by phase separation ("phase separation method"),[28] and subsequent calcination under an inert atmosphere allows for

Received: December 11, 2014
Published: March 2, 2015

DOI: 10.1021/ic502972v
Inorg. Chem. 2015, 54, 2802−2808

conversion into reduced Ti phases while preserving the macroporous structure.[25] Although the reduction of TiO_2 provides a mixture of Ti_nO_{2n-1} phases, in most cases,[1,10,21] we have found that Ti_4O_7, Ti_3O_5, and TiO_xN_y are selectively obtained as a single phase depending on the calcination temperature via the preceramic polymer route from titanium ethylenediamine based monolithic gels.[25] Elemental analysis has revealed that the resultant reduced titanium oxides are doped with N atoms due to the diamine-bridged preceramic compound, and the effects of N doping on the distinguished crystallization behavior have been investigated.

In this study, we focus on the effect of calcination conditions, especially the atmosphere, on various characteristics of the resultant materials, such as the pore properties, crystal phase, degree of N doping, and bulk conductivity. In the systems described herein, three different calcination conditions were employed; (I) under Ar gas flow; (II) in a loosely closed crucible under Ar gas flow: (III) under N_2 gas flow. In an effluent Ar stream, the gaseous species emanating from the preceramic polymers during calcination are rapidly removed, whereas they stay around the specimen in a closed crucible. A comparison of the results under those two conditions gives an account for reaction by the gases generated from the specimen. In the presence of N_2, on the other hand, nitridation takes place concomitantly with carbothermal reduction.[21,22] The three systems delivered obvious differences in the phase transition tendency and various characteristics of the resultant materials. In light of the obtained results, impacts of the calcination conditions on the features of the final products are discussed.

2. EXPERIMENTAL PROCEDURES

2.1. Sample Preparation. The precursor gels were prepared by the phase separation method reported previously.[25] In a typical synthesis, 5.0 mL of titanium *n*-propoxide [$Ti(OPr)_4$; Sigma-Aldrich Co.], 2.0 mL of 1-propanol (PrOH; Tokyo Chemical Industry Co., Ltd.), and 1.84 mL of acetylacetone (AcAc; Tokyo Chemical Industry Co., Ltd.) were mixed in a glass tube. After a homogeneous yellow solution was obtained, 0.325 g of poly(ethylene glycol) (PEG; M_v = 10000, Sigma-Aldrich Co.) was added followed by stirring at 60 °C to dissolve PEG completely. Then, 2.5 mL of ethylenediamine (EDA; Sigma-Aldrich Co.) was added slowly with vigorous stirring at 60 °C. After mixing for 1 min, the obtained homogeneous solution was kept at 60 °C for 24 h for gelation and aging. The molar ratio of $Ti(OPr)_4$/AcAc/EDA was fixed as 1:1.0:2.1 unless otherwise noted. The resultant wet gels were subsequently dried at 60 °C for 48 h and then thoroughly dried under vacuum at 60 °C for 48 h to obtain the Ti-based inorganic−organic hybrid xerogels. The samples were stored in a vacuum desiccator to avoid hydrolysis by moisture in air.

The resultant xerogels were calcined at various temperatures for 4 h with a heating rate of 4 °C min^{-1} in an effluent Ar or N_2 gas stream at a rate of 1.0 L min^{-1} in an tubular furnace, which had been purged with Ar in advance to completely remove air inside the pores of the samples. Some samples were calcined in a crucible loosely closed with a lid under an Ar atmosphere, where they were closed to the external environment. The sample codes were given as Ar-*T* and N_2-*T* for the samples calcined under Ar and N_2 atmospheres and C-*T* for the samples calcined in a closed crucible, where *T* is assigned as the calcination temperature.

2.2. Characterization. The microstructures of the fractured surfaces of the samples were observed using scanning electron microscopy (SEM; JSM-6060S, JEOL), field-emission SEM (FE-SEM; JSM-6700F, JEOL), and transmission electron microscopy (TEM; JEM-2010DM, JEOL). A N_2 physisorption apparatus (BELSORP-mini II, Bel Japan Inc.) was employed to characterize the micro- and mesoporous properties. Helium pycnometry (Pentapyc 5200e, Quantachrome Instruments) was employed to determine the skeletal densities. Before N_2 sorption measurement and helium pycnometry, the sample was degassed at 200 °C under vacuum. Bulk densities were calculated as [weight]/[bulk volume]. The porosity (%) of each sample was calculated as $(1 - \rho_b/\rho_s) \times 100$, where ρ_b and ρ_s are bulk and skeletal densities, respectively. The crystal structure was confirmed by powder X-ray diffraction (XRD; RINT Ultima III, Rigaku Corp.) using Cu Kα (λ = 0.154 nm) as an incident beam. Elemental analysis of the samples was carried out by X-ray photoelectron spectroscopy (XPS; MT-5500, ULVAC-PHI, Inc.). Monochromatized X-ray Mg Kα radiation (1253.6 eV) was used. The core levels were calibrated by reference to the first component of the C 1s core-level peak (unfunctionalized hydrocarbons) set at 284.6 eV. X-ray absorption near-edge spectroscopy (XANES) was performed at the Ti K-edge to explore the valence state of the Ti atom in the samples calcined under different conditions. XANES measurements were carried out in transmission mode with a Si(111) monochromator on Beamline 20-BM at APS, Argonne National Laboratory. The samples diluted with boron nitride were pressed into pellets and enwrapped with Kapton tape for the measurements. As a reference, commercial TiO_2, Ti_2O_3, TiN, and TiO (Sigma-Aldrich Co.) were also measured. The reference Ti XANES spectrum was collected simultaneously from a Ti metal foil in the reference channel, and the energy calibration of each spectrum was performed by aligning the first derivative maximum of the Ti metal XANES spectrum in the reference channel to the literature value of 4966 eV. All of the XANES data were processed using standard preedge background subtraction and edge-step normalization procedures using the *ATHENA* program. Thermogravimetry (TG) was performed by Thermo plus TG 8120 (Rigaku Corp.) at a heating rate of 5 °C min^{-1} with air continuously supplied at a rate of 100 mL min^{-1}. The electric conductivities of the monolithic electrodes were measured by the four-probe method using a Physical Property Measurement System (PPMS, Quantum Design). The apparent cross-sectional area of the monolithic electrode was used for evaluation of the obtained conductivity values.

3. RESULTS AND DISCUSSION

The preceramic polymer route to obtain porous Ti-based ceramics is illustrated in Figure 1. Macroporous EDA-bridged Ti-based inorganic−organic hybrid gels can be fabricated via the nonaqueous sol−gel process accompanied by phase separation.[25] As reported previously,[25] the subsequent calcination of the preceramic polymer under an Ar atmosphere first

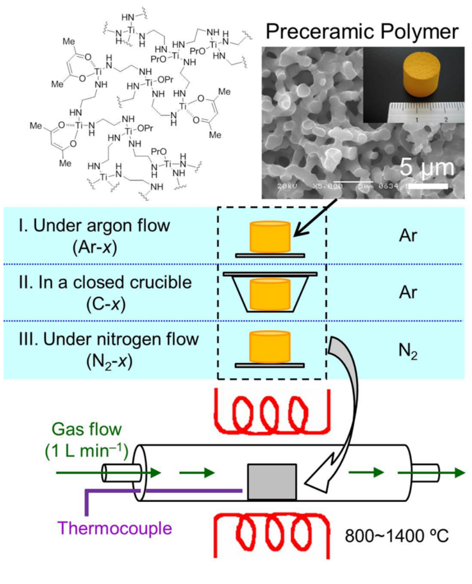

Figure 1. Scheme showing the sol−gel synthesis of macroporous EDA-bridged Ti-based gels and the conversion into porous monoliths based on reduced titanium oxides.

produces N-doped TiO_2/C composites, which are subsequently reduced to a series of titanium oxide phases by carbothermal reduction. Here, both the titanium oxide and carbon moieties are doped with N atoms due to the N-rich preceramic polymer network. Further reduction and nitridation take place with elevation of the temperature, and the transition into the cubic phase takes place at around 1200 °C. In this study, we have further investigated two other calcination conditions (closed and N_2 atmospheres) and compared various characteristics of the resultant samples.

3.1. Difference in the Pore Properties with Varied Calcination Conditions. Regarding the pore properties, we focus on the difference between the samples calcined under Ar and N_2 atmospheres. Upon calcination of the preceramic polymer gel under a N_2 atmosphere, both the monolithic structure and the interconnected macroporous morphology can be retained up to 1400 °C (Figure 2), as is the case under the Ar atmosphere reported previously.[25] The micro- and mesopore properties were examined by N_2 physisorption measurement and summarized in Figure 3 and Table 1. The change of the nitrogen isotherms of the N_2-T samples upon increasing calcination temperature shows a similar tendency to the Ar-T samples. All of the samples calcined below 1000 °C exhibit a sharp uptake at low relative pressures followed by reaching of a plateau (type I isotherm), which is represented by the microporous property derived from the carbon species.[25] When the calcination temperature is higher than 1200 °C, however, the shapes of the isotherms appear to be different between the two conditions. The uptake is shifted to lower relative pressure in N_2-1200 compared to Ar-1200, which indicates that there are smaller mesopores in N_2-1200. In the case of the samples calcined at 1400 °C, Ar-1400 shows almost no uptake over the complete range, while there are small uptakes in N_2-1400, leading to the higher specific surface area, as shown in Table 1.

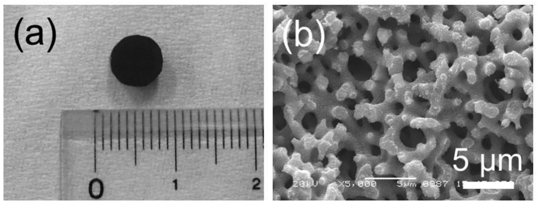

Figure 2. (a) Appearance and (b) macroporous morphology of N_2-1400.

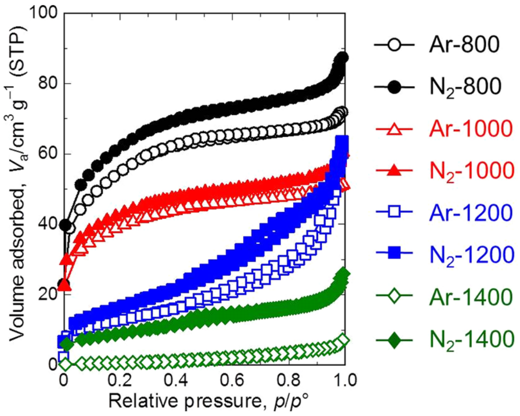

Figure 3. Comparison between the N_2 adsorption−desorption isotherms of the samples calcined at different temperatures under Ar and N_2 atmospheres.

Table 1. Pore Properties of the Samples Calcined at Different Temperatures

	S_{BET}[a] (m^2 g^{-1})	$V_{micromeso}$[b] (cm^3 g^{-1})	ρ_b[c] (g cm^{-3})	ρ_s[d] (g cm^{-3})	porosity[e] (%)
Ar-800	198	0.111	1.29	3.48	63
Ar-1000	143	0.080	1.43	3.76	62
Ar-1200	45	0.090	1.56	4.47	65
Ar-1400	<5	0.011	1.62	4.80	66
N_2-800	224	0.134	1.30	3.20	59
N_2-1000	156	0.093	1.52	3.80	60
N_2-1200	60	0.097	1.64	4.25	61
N_2-1400	32	0.039	1.78	4.72	62

[a] Specific surface area obtained by the Brunauer−Emmett−Teller method. [b] Micro- and mesopore volumes obtained by N_2 adsorption isotherms at $p/p_0 = 0.99$. [c] Bulk density calculated as [weight]/[bulk volume]. [d] Skeletal density measured by helium pycnometry. [e] Calculated by $100(1 - \rho_b/\rho_s)$.

The nanostructural difference between the samples calcined at 1200 °C can be observed by electron microscopy on the cross sections of the macropore skeletons (Figure 3). The macropore skeletons of the samples are composed of particle agglomerates, whose interstices correspond to mesopores. It is found that the particle size of N_2-1200 is obviously smaller than that of Ar-1200, leading to the smaller mesopores in N_2-1200. TEM observation (Figure 4c,d) reveals that N_2-1200 is composed of smaller crystallites (about 10−40 nm), whereas Ar-1200 comprises larger crystallites with a size of ~100 nm. The results indicate that the calcination atmosphere affects crystal growth during thermal treatment, leading to differences in the pore properties and crystal size. This point will be discussed later.

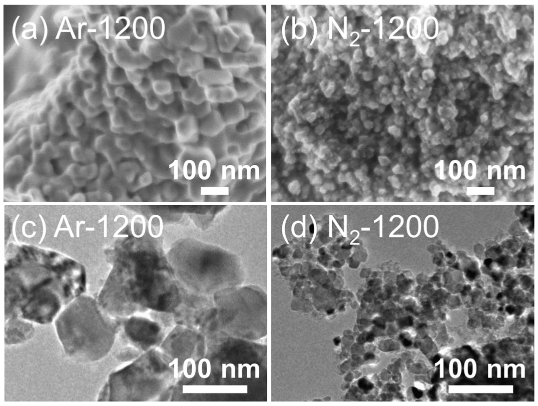

Figure 4. (a and b) FE-SEM images of the cross section of the macropore skeletons. (c and d) TEM images of the samples calcined at 1200 °C. (a and c) Ar-1200; (b and d) N_2-1200.

The porosities of the samples calculated from the bulk and skeletal densities are also given in Table 1. Both the bulk and skeletal densities increase with increasing calcination temperature. Although the porosity generally decreases at higher temperature, the estimated porosity does not decrease but slightly increases with increasing calcination temperature in all of the systems. This is presumably because the macropore skeleton was reinforced via sintering at higher temperature, which mitigated shrinkage during the holding time for calcination.[29] In such macroporous monolithic materials, the decrement of the porosity is predominantly affected by shrinkage of the macropores, which occurs not only with increasing temperature but also during the retention period for calcination. It is deduced that the macropore skeleton during calcination is more reinforced when the calcination temperature is higher, leading to smaller shrinkage of the macroporous structure during the retention period. As a result, over 60% of the porosity still remains even after calcination at 1400 °C.

3.2. Difference in the Crystal Transition Behavior under Different Calcination Conditions.

The crystal transition behavior upon heating under different conditions investigated by the XRD profiles (Figure S1 in the Supporting Information, SI) is summarized in Table 2. The samples calcined in a closed crucible (C-*T*) exhibit crystallization behavior similar to that of Ar-*T* samples. Meanwhile, the peaks assigned to the rock-salt structure of TiO_xN_y appear in all N_2-*T* samples. In other words, although crystallization into TiO_xN_y generally occurs at higher than 1100 °C in the case of carbothermal reduction of TiO_2 under a N_2 atmosphere,[21] the present preceramic polymer route allows it at as low as 800 °C. Crystallization of TiN at 800 °C was also reported in the preceramic polymer route of titanium hydrazide hybrid networks by Kim and Kumta.[30] They put forward that the TiN crystal phase arises from the network that comprises direct bonding of Ti and N. In our case, however, almost no diffraction peaks of cubic TiO_xN_y are detected in the Ar-*T* and C-*T* samples, which implies that only a few TiO_xN_y were formed directly from the hybrid network and/or via reaction with the generated gases, such as NH_3 and NO.[25] It is therefore reasonable that carbothermal reduction and nitridation with N_2 of titanium oxides took place at ~800 °C in the present preceramic polymer route under a N_2 atmosphere. In the previous study,[25] we already discussed the lower stability of N-doped TiO_2 caused by O−Ti−O lattice distortion with interstitial and/or substitutional N atoms.[31] Hence, the inherently N-doped Ti−O lattice derived from diamine-bridged Ti-based preceramic polymer networks is more susceptible to nitridation by N_2 at ~800 °C, while it is not high enough for nitridation of undoped TiO_2.[21] In addition, nevertheless, the transformation from Ti_4O_7 to γ-Ti_3O_5 occurred in Ar-1000 and C-1000, and the crystal phase of N_2-1000 still remained Ti_4O_7. It is also worth noting that no peaks of Ti_2O_3 are detected in N_2-1200, whereas Ar-1200 and C-1200 contain a substantial amount of Ti_2O_3.

Table 2. Phase Compositions of the Samples Calcined under Different Conditions

temperature (°C)	Ar-*T*[a]	C-*T*	N_2-*T*
800	Ti_4O_7	Ti_4O_7	Ti_4O_7, TiO_xN_y
1000	γ-Ti_3O_5	γ-Ti_3O_5	Ti_4O_7, TiO_xN_y
1200	TiO_xN_y, Ti_2O_3	TiO_xN_y, Ti_2O_3	TiO_xN_y
1400	TiO_xN_y	TiO_xN_y, Ti_2O_3[b]	TiO_xN_y, β-Ti_3O_5[b]

[a] From ref 25. [b] Trace.

Elemental analysis was conducted by XPS for the detailed investigation of the amount of N atoms in each sample, and the results are compiled in Figures 5 and S2 in the SI. The N 1s core-level spectra of the samples (Figure 5) show two components around 394.5−398.5 and 398.5−403 eV. The peak centered at 396.6 eV is assigned to the N−Ti bond (substitutional N atoms).[32,33] Meanwhile, the band around 398−403 eV is attributed to N-related functionalities in C.[34] A peak derived from interstitial N atoms in the Ti−O lattice also appears at ~400 eV.[35] These components are, however, hardly distinguished. In all of the systems, enhancement of the peak at 396.6 eV together with diminution of the peak around 400 eV is observed, which reflects an increase in the amount of the N−Ti bond and a decrease in the amounts of N-doped C and interstitial N atoms.

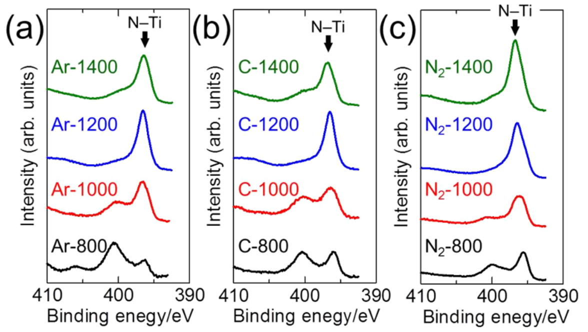

Figure 5. N 1s XPS spectra of the samples calcined at different temperatures: (a) Ar-*T*; (b) C-*T*; (c) N_2-*T*.

The N/Ti molar ratios of the calcined samples were estimated from the XPS spectra, as shown in Table 3. The degrees of nitridation ([N−Ti]/Ti) were also evaluated by the deconvolution of the N 1s spectra. It is found that the amount of substitutional N atoms ([N−Ti]/Ti) of C-800 is relatively larger than that of Ar-800. This indicates that the gases evolved from the N-doped carbonaceous species contributed to formation of the Ti−N bonds to some extent at 800 °C. On the other hand, the [N−Ti]/Ti ratios of Ar-*T* and C-*T* become similar when *T* is higher than 1000. We therefore suppose that the interstitial N atoms in the Ti−O lattice convert to substitutional N atoms above 1000 °C. When the samples were calcined under a N_2 atmosphere, both N/Ti and [N−Ti]/Ti become much larger than those of the other systems because of nitridation by N_2 as mentioned above. The noticeably larger value of [N−Ti]/Ti in N_2-1000 compared to Ar-1000 and C-1000 indicates that cubic TiO_xN_y was formed near the surface of the crystal grains because the surface is increasingly more exposed to N_2 gas.

As for the Ti 2p spectra in Figure S2a in the SI, two prominent peaks at 464.7 and 459.0 eV, which are attributed to Ti $2p_{1/2}$ and Ti $2p_{3/2}$ of Ti−O for Ti^{IV}, are observed in the samples calcined below 1000 °C. When the calcination temperature is higher (>1200 °C), the peak shape becomes more complicated with bands (or shoulders) at lower binding energy. These components include doublet peaks assigned to Ti $2p_{1/2}$ and Ti $2p_{3/2}$ of Ti−N, Ti−C, and Ti−O for Ti^{III} and Ti^{II}.[32,33,36] Although it is difficult to determine the molar ratios of each component, it is found that the band related to the reduced states of Ti appears in all of the samples calcined above 1200 °C. In the cases of Ar-*T* and C-*T*, the intensity of the lower-binding energy peak (~455 eV) decreases when the calcination temperature increases from 1200 to 1400 °C. This result indicates that the surface oxidation of crystallites takes place at 1400 °C. According to the C 1s spectra presented in Figure S2b in the SI, Ti−C bonds are formed on the surface in these samples, which is confirmed by the peak at 281.6 eV (C−Ti).[36] As reported previously,[25] the XRD result reveals that the

Table 3. Surface Elemental Ratios of the Samples Calcined at Different Conditions

	N/Ti[a]	[N–Ti]/Ti[b]		N/Ti[a]	[N–Ti]/Ti[b]		N/Ti[a]	[N–Ti]/Ti[b]
Ar-800[c]	0.14	0.034	C-800	0.26	0.10	N_2-800	0.40	0.17
Ar-1000[c]	0.20	0.12	C-1000	0.23	0.12	N_2-1000	0.38	0.31
Ar-1200[c]	0.26	0.21	C-1200	0.26	0.19	N_2-1200	0.90	0.79
Ar-1400[c]	0.22	0.17	C-1400	0.18	0.14	N_2-1400	0.90	0.81

[a] Molar ratio of N/Ti in the whole N-doped titanium oxide/carbon composites obtained from the XPS spectra. [b] Amount of N atoms bonding to Ti atoms in the crystal lattice of titanium oxides estimated by deconvolution of the N 1s spectra. [c] From ref 25.

Ti–C bonds are distributed only near the outermost surface and that the amount of titanium oxycarbides (or carbides) is negligible in bulk. The peak intensity of Ti–C becomes lower in Ar-1400 and C-1400, which is consistent with the diminished peak at 455 eV.

On the other hand, the Ti 2p spectra of N_2-1200 and N_2-1400 are similar, and there are no peaks attributed to Ti–C in the C 1s spectra. It was reported that titanium oxycarbide is formed above 1000–1100 °C during carbothermal reduction,[37,38] indicating that Ti–C bonds are supposed to be formed in the samples calcined above 1200 °C. In a N_2 atmosphere, crystallization to TiN starts in the early stage of calcination (~800 °C) ahead of the formation of Ti–C bonds. It is therefore deduced that Ti–C bonds are more likely to be formed from Ti–O than from Ti–N. Another plausible reason is that the reduction to TiO_xN_y ran out of C atoms, resulting in only a few Ti–C bonds developed in the N_2 stream.

In contrast to surface analysis by XPS, XANES analysis was also carried out in order to investigate the valence of Ti in the whole sample, as presented in Figure 6. As observed in the Ti K-edge spectra of the series of Ti standard compounds, the edge onset energy shifts to the lower value with a decrease in the valence of Ti (TiO_2, Ti^{IV}; Ti_2O_3 and TiN, Ti^{III}; TiO, Ti^{II}), which reflects the decrease in the binding energy of the Ti 1s electron.[39] The spectra of Ti_2O_3 and TiN, which are both derived from Ti^{III}, also show some difference because of the differences of the crystal structure. As for the specimens prepared in this study, the negative shift of the edge energy position with increasing calcination temperature is observed under all atmospheric conditions. These results are consistent with the aforementioned characterizations.

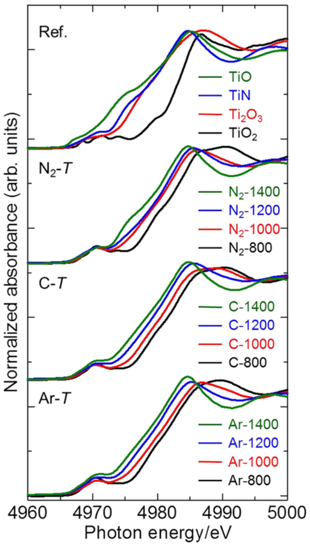

Figure 6. Ti K-edge XANES spectra for the reference samples (TiO, TiN, Ti_2O_3, and TiO_2) and the samples calcined under different conditions.

The proportion of Ti valence can be approximated by the linear combination fitting (by the *ATHENA* software program) using the spectra of Ti standards. The estimation of the Ti^{IV}/Ti^{III} ratios for the samples calcined below 1000 °C is given in Table S1 in the SI. It should be taken into account that the fitting results are just approximations because titanium oxides in the samples were subjected to N doping as described above. Nevertheless, the tendency of the relationship between the calcination conditions and the Ti^{IV}/Ti^{III} ratios seems to be reasonable. For instance, the Ti^{IV}/Ti^{III} ratios of the samples calcined at 800 °C whose dominant phase is Ti_4O_7 are around 1.7, which is close to 2 of the ideal Ti^{IV}/Ti^{III} ratio for Ti_4O_7. With increasing calcination temperature to 1000 °C, the Ti^{IV}/Ti^{III} ratios clearly decrease. Considering the main crystal phase in each sample (see Table 2), the values appear to be small, which is probably due to N doping. In particular, the Ti^{IV}/Ti^{III} ratio of N_2-1000 is the lowest (~0.4) because it contains TiN crystallites.

We also applied the fitting evaluation to the samples calcined at 1400 °C, which are mostly composed of cubic TiO_xN_y, in order to assess the values of x and y. Here, TiO and TiN were used as standards, and it is assumed that $x + y = 1$. The x/y proportions estimated by XANES are demonstrated in Table 4.

Table 4. Bulk Composition of the TiO_xN_y Specimens Calcined at 1400 °C Estimated by Fitting the XANES Spectra Using TiO and TiN as References[a]

	x (TiO)	y (TiN)
Ar-1400	0.11	0.89
C-1400	0.09	0.91
N_2-1400	0.01	0.99

[a] It is assumed that $x + y = 1$.

It is worth noting that the bulk compositions of TiO_xN_y crystallites in Ar-1400 and C-1400 are close to $TiO_{0.1}N_{0.9}$, even when the [N–Ti]/Ti ratios of the crystal surface are less than 0.2. In the case of N_2-1400, in contrast, the surface composition is estimated as about $TiO_{0.2}N_{0.8}$ by XPS, and the XANES spectrum almost corresponds to that of TiN.

3.3. Insights into the Effect of the Calcination Atmosphere on Crystal Growth and Phase Transition.

In general, the preceramic polymer route in an inert atmosphere provides ceramics as a composite with C, which is derived from decomposition of the organic moieties of a precursor polymer.[26,27,30,40] With increasing temperature, the C atoms are consumed by carbothermal reduction, followed by the formation of carbides in some cases.[26,27,40] In the system described herein, the N-containing networks gave rise to N-doped C atoms. TG analysis (Figure S3 in the SI) disclosed that the C species remained up to 1000 °C under Ar and N_2

atmospheres, while C-1200 still included a substantial amount of C. Taking these results into account, the factors that induce the difference in the phase transition behavior as well as crystal growth are discussed as follows.

The most significant difference between the calcination systems under Ar and N_2 atmospheres is the dominant crystal phase in the samples calcined at 1000 °C: Ti_3O_5 for Ar-1000 and Ti_4O_7 for N_2-1000. One of the plausible reasons is that the cubic TiO_xN_y formed on the surface of the crystallites hinders carbothermal reduction into Ti_3O_5 at 1000 °C by intervening with the contact of Ti_4O_7 with C. In addition, even if Ti_3O_5 was formed, subsequent conversion into TiO_xN_y was likely to take place, which is also suggested from the thermodynamical and experimental points of view in the previous literature.[21] It is also deduced that this TiO_xN_y shell might suppress crystal growth, which led to smaller crystallites in N_2-1200 than Ar-1200, as observed in Figure 4. Crystal growth of TiO_xN_y is presumably slower than that of Ti_nO_{2n-1} because of the higher thermal stability.

The absence of Ti_2O_3 in N_2-1200 is also a distinguished difference in the crystal transition behavior compared to calcination under an Ar atmosphere. In the previous literature, Berger[22] demonstrated the instability of Ti_2O_3 under carbothermal conditions with N_2 gas, but no clear explanation was given on this phenomenon. His experimental results show the formation of the cubic phase and β-Ti_3O_5 from the Ti_2O_3/C mixtures after calcination under N_2 at 1400 °C, which is consistent with the trace of β-Ti_3O_5 detected in N_2-1400 (Figure S1b in the SI). We therefore put forward that once Ti_2O_3 is formed as an intermediate between 1000 and 1200 °C, it is then transformed into TiO_xN_y through nitridation by N_2, which is also supported by thermodynamic calculation.[21]

3.4. Electric Conductivities of Monolithic Electrodes Calcined under Different Conditions. Figure 7 shows a comparison of the temperature-dependent electric conductivities for the monolithic samples calcined under Ar and N_2 atmospheres. The samples calcined at 800 °C exhibit a semiconducting behavior, which reflects the conductive feature of C. It is therefore speculated that the N-doped titanium oxide crystallites were separately embedded in the C matrix. The low crystallinity might be another reason. Meanwhile, the anomalies around ~250 and ~150 K are observed in Ar-1000 and N_2-1000, respectively. The former is derived from the reversible structural transition of γ-Ti_3O_5 and δ-Ti_3O_5,[41] and the latter is a Peierls-like metal–insulator transition of Ti_4O_7.[42] The conductivities of the samples calcined above 1200 °C are less affected by temperature, like metallic behavior. Because a negligible amount of C remaine in these samples, the electric conductivity behaviors of the monoliths directly reflect the feature of TiO_xN_y.[43] In particular, N_2-1200 and N_2-1400 deliver excellent conductivities of ~380 S cm^{-1} along with the superconducting transition at around 4 K (see Figure S4 in the SI). The superconducting transition temperature (T_c) of cubic TiO_xN_y decreases as y decreases; i.e., T_c = 6.0 and <0.02 K for y = 0.99 and 0.80, respectively.[44,45] Although the bulk composition of TiO_xN_y in Ar-1400 is close to $TiO_{0.1}N_{0.9}$ as shown in Table 4, the incorporation of Ti–C on the crystallite surface causes a loss of the superconducting transition.

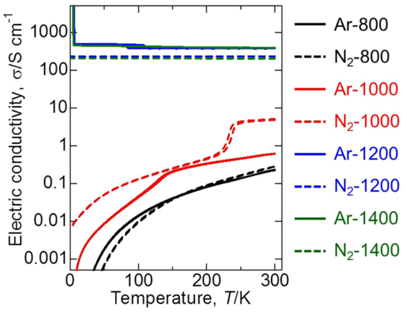

Figure 7. Temperature–electric conductivity relationship of the monolithic samples calcined at different temperatures under Ar and N_2 atmospheres.

4. CONCLUSIONS

The current work specifies the effect of calcination conditions on various properties of the porous monolithic materials prepared via the preceramic polymer route from EDA-bridged Ti-based gels, that is, porous N-doped reduced titanium oxides and oxynitrides. It has been found that the atmospheric conditions during calcination have widespread influence on the crystal growth and phase transition tendency, all of which lead to differences in the micro- and mesoporous properties as well as electric conductivity. Calcination under a N_2 atmosphere allows nitridation at as low as 800 °C, which suppresses crystal growth. As a result, the porous TiO_xN_y monolith calcined at 1200 °C under a N_2 atmosphere is composed of smaller crystallites, leading to higher specific surface area compared to that treated under an Ar atmosphere. In addition, TiO_xN_y developed on the grain surface below 1000 °C prevents the formation of a surface layer based on oxycarbides, which impairs the electric conductivity.

■ ASSOCIATED CONTENT

Ⓢ Supporting Information

XRD patterns, XPS spectra, ratios of Ti^{IV}/Ti^{III} in the samples calcined under different conditions, TG curves, and bulk resistivity as a function of the temperature of the samples. This material is available free of charge via the Internet at http://pubs.acs.org.

■ AUTHOR INFORMATION

Corresponding Author

*E-mail: h-george@elech.kuic.kyoto-u.ac.jp.Tel: +81 753 832 126. Fax: +81 753 832 488.

Notes

The authors declare no competing financial interest.

■ ACKNOWLEDGMENTS

The present work was supported by a Grant-in-Aid for JSPS Fellows (Grant 24·31 to G.H.) from the Japan Society for the Promotion of Science (JSPS). PNC/XSD facilities at the APS and research at these facilities are supported by the U.S. Department of Energy (DOE), Basic Energy Sciences, the Canadian Light Source and its funding partners, the University of Washington, and the APS. Use of the APS, an Office of Science User Facility, operated for the U.S. DOE, Office of Science, by Argonne National Laboratory was supported by the U.S. DOE under Contract DE-AC02-06CH11357.

■ REFERENCES

(1) Gusev, A. A.; Avvakumov, E. G.; Medvedev, A. Zh.; Masliy, A. I. *Sci. Sintering* **2007**, *39*, 51–57.

(2) Ioroi, T.; Senoh, H.; Yamazaki, S.; Siroma, Z.; Fujiwara, N.; Yasuda, K. *J. Electrochem. Soc.* **2008**, *155*, B321−B326.
(3) Walsh, F. C.; Wills, R. G. A. *Electrochim. Acta* **2010**, *55*, 6342−6351.
(4) Li, X.; Zhu, A. L.; Wang, H.; Hui, R.; Zhang, L.; Zhang, J. *Electrochim. Acta* **2010**, *55*, 5891−5898.
(5) Choi, D.; Kumta, P. N. *J. Electrochem. Soc.* **2006**, *153*, A2298−A2303.
(6) Jiang, Q. W.; Li, G. R.; Gao, X. P. *Chem. Commun.* **2009**, *44*, 6720−6722.
(7) Lu, X.; Wang, G.; Zhai, T.; Yu, M.; Xie, S.; Ling, Y.; Liang, C.; Tong, Y.; Li, Y. *Nano Lett.* **2012**, *12*, 5376−5381.
(8) Iwasaki, H.; Bright, N. F. H.; Rowland, J. F. *J. Less-Common Met.* **1969**, *17*, 99−110.
(9) Wahlbeck, P. G.; Gilles, P. W. *J. Am. Ceram. Soc.* **1966**, *49*, 180−183.
(10) Hauf, C.; Kniep, R.; Pfaff, G. *J. Mater. Sci.* **1999**, *34*, 1287−1292.
(11) Kitada, A.; Hasegawa, G.; Kobayashi, Y.; Kanamori, K.; Nakanishi, K.; Kageyama, H. *J. Am. Chem. Soc.* **2012**, *134*, 10894−10898.
(12) Andersson, S.; Collén, B.; Kuylenstierna, U.; Magnéli, A. *Acta Chem. Scand.* **1957**, *11*, 1641−1652.
(13) Le Roux, H.; Glasser, L. *J. Mater. Chem.* **1997**, *7*, 843−851.
(14) Zukalova, M.; Prochazka, J.; Bastl, Z.; Duchoslav, J.; Rubacek, L.; Havlicek, D.; Kavan, L. *Chem. Mater.* **2010**, *22*, 4045−4055.
(15) Ohkoshi, S.; Tsunobuchi, Y.; Matsuda, T.; Hashimoto, K.; Namai, A.; Hakoe, F.; Tokoro, H. *Nat. Chem.* **2010**, *2*, 539−545.
(16) Kwon, D. H.; Kim, K. M.; Jang, J. H.; Jeon, J. M.; Lee, M. H.; Kim, G. H.; Li, X. S.; Park, G. S.; Lee, B.; Han, S.; Kim, M.; Hwang, C. S. *Nat. Nanotechnol.* **2010**, *5*, 148−153.
(17) Toyoda, M.; Yano, T.; Tryba, B.; Mozia, S.; Tsumura, T.; Inagaki, M. *Appl. Catal., B* **2009**, *88*, 160−164.
(18) Lazarov, M.; Raths, P.; Metzger, H.; Spirkl, W. *J. Appl. Phys.* **1995**, *77*, 2133−2137.
(19) Fischer, A.; Makowski, P.; Müller, J. O.; Antonietti, M.; Thomas, A.; Goettman, F. *ChemSusChem* **2008**, *1*, 444−449.
(20) Kaskel, S.; Schlichte, K.; Kratzke, T. *J. Mol. Catal. A: Chem.* **2004**, *208*, 291−298.
(21) White, G. V.; Mackenzie, K. J. D.; Brown, I. W. M.; Bowden, M. E.; Johnston, J. H. *J. Mater. Sci.* **1992**, *27*, 4294−4299.
(22) Berger, L. M. *J. Mater. Sci.* **2001**, *20*, 1845−1848.
(23) Newman, J.; Tiedeman, W. *AIChE J.* **1975**, *21*, 25−41.
(24) Hasegawa, G.; Kitada, A.; Kawasaki, S.; Kanamori, K.; Nakanishi, K.; Kobayashi, Y.; Kageyama, H.; Abe, T. *J. Electrochem. Soc.* **2015**, *162*, A77−A85.
(25) Hasegawa, G.; Sato, T.; Kanamori, K.; Nakano, K.; Yajima, T.; Kobayashi, Y.; Kageyama, H.; Abe, T.; Nakanishi, K. *Chem. Mater.* **2013**, *25*, 3504−3512.
(26) Bill, J.; Aldinger, F. *Adv. Mater.* **1995**, *7*, 775−787.
(27) Colombo, P.; Mera, G.; Riedel, R.; Sorarù, G. D. *J. Am. Ceram. Soc.* **2010**, *93*, 1805−1837.
(28) Nakanishi, K. *J. Porous Mater.* **1997**, *4*, 67−112.
(29) Hasegawa, G.; Kanamori, K.; Nakanishi, K.; Hanada, T. *Carbon* **2010**, *48*, 1757−1766.
(30) Kim, I. S.; Kumta, P. N. *Mater. Sci. Eng., B* **2003**, *B98*, 123−134.
(31) Jagadale, T. C.; Takale, S. P.; Sonawane, R. S.; Joshi, H.; Patil, S. I.; Kale, B. B.; Ogale, S. B. *J. Phys. Chem. C* **2008**, *112*, 14595−14602.
(32) Bertóti, I.; Mohai, M.; Sullivan, J. L.; Saied, S. O. *Appl. Surf. Sci.* **1995**, *84*, 357−371.
(33) Nowak, A. M.; McCreey, R. L. *Anal. Chem.* **2004**, *76*, 1089−1097.
(34) Pels, J. R.; Kapteijn, F.; Moulijn, J. A.; Zhu, Q.; Thomas, K. M. *Carbon* **1995**, *33*, 1641−1653.
(35) Di Valentin, C.; Pacchioni, G.; Selloni, A.; Livraghi, S.; Giamello, E. *J. Phys. Chem. B* **2005**, *109*, 11414−11419.
(36) Voevodin, A. A.; Capano, M. A.; Laube, S. J. P.; Donley, M. S.; Zabinski, J. S. *Thin Solid Films* **1997**, *298*, 107−115.
(37) Preiss, H.; Berger, L. M.; Schultze, D. *J. Eur. Ceram. Soc.* **1999**, *19*, 195−206.
(38) Koc, R. *J. Eur. Ceram. Soc.* **1997**, *17*, 1309−1315.
(39) Graetz, J.; Reilly, J. J.; Johnson, J.; Ignatov, A. Y.; Tyson, T. A. *Appl. Phys. Lett.* **2004**, *85*, 500−502.
(40) Hasegawa, G.; Kanamori, K.; Nakanishi, K.; Hanada, T. *Chem. Mater.* **2010**, *22*, 2541−2547.
(41) Hong, S. H.; Åsbrink, S. *Acta Crystallogr.* **1982**, *B38*, 2570−2576.
(42) Lakkis, S.; Schlenker, C.; Chakraverty, B. K.; Buder, R. *Phys. Rev. B* **1976**, *14*, 1429−1440.
(43) Martin, N.; Banakh, O.; Santo, A. M. E.; Springer, S.; Sanjinés, R.; Takadoum, J.; Lévy, F. *Appl. Surf. Sci.* **2001**, *185*, 123−133.
(44) Spengler, W.; Kaiser, R.; Christensen, A. N.; Müller-Vogt, G. *Phys. Rev. B* **1978**, *17*, 1095−1101.
(45) Höchst, H.; Bringans, R. D.; Steiner, P.; Wolf, Th. *Phys. Rev. B* **1982**, *25*, 7183−7191.